

Inverse Design and Experimental Verification of a Bianisotropic Metasurface Using Optimization and Machine Learning

Stewart Pearson¹, Graduate Student Member, IEEE, Parinaz Naseri¹, Graduate Student Member, IEEE, AND Sean V. Hum¹, Senior MEMBER, IEEE

¹The Edward S. Rogers Sr. Department of Electrical & Computer Engineering, University of Toronto, Toronto, ON, Canada, M5S 3G8

CORRESPONDING AUTHOR: Stewart Pearson (e-mail: stewart.pearson@mail.utoronto.ca).

IEEE OJAP encourages responsible authorship practices and the provision of information about the specific contribution of each author

This work was supported by the Natural Sciences and Engineering Research Council (NSERC) of Canada.

ABSTRACT Electromagnetic metasurfaces have attracted significant interest recently due to their low profile and advantageous applications. Practically, many metasurface designs start with a set of constraints for the radiated far-field, such as main-beam direction(s) and side lobe levels, and end with a non-uniform physical structure for the surface. This problem is quite challenging, since the required tangential field transformations are not completely known when only constraints are placed on the scattered fields. Hence, the required surface properties cannot be solved for analytically. Moreover, the translation of the desired surface properties to the physical unit cells can be time-consuming and difficult, as it is often a one-to-many mapping in a large solution space. Here, we divide the inverse design process into two steps: a macroscopic and microscopic design step. In the former, we use an iterative optimization process to find the surface properties that radiate a far-field pattern that complies with specified constraints. This iterative process exploits non-radiating currents to ensure a passive and lossless design. In the microscopic step, these optimized surface properties are realized with physical unit cells using machine learning surrogate models. The effectiveness of this end-to-end synthesis process is demonstrated through measurement results of a beam-splitting prototype.

INDEX TERMS Deep neural networks, bianisotropy, electromagnetic metasurfaces, surface waves, inverse design, machine learning, non-uniform metasurface, optimization, surrogate models.

I. INTRODUCTION

ELECTROMAGNETIC metasurfaces (EMMSs) are electrically-thin surfaces that enable exotic field transformations [1]. These field transformations are accomplished by manipulating the generalized sheet transition conditions (GSTCs), which relate the fields on one side of the surface to the other through the surface parameters [2]. Bianisotropic magneto-electric and electro-magnetic coupling terms can also be leveraged as a degree of freedom to implement any desired power-conserving field transformation. The surface parameters are typically realized by sub-wavelength meta-

atoms composed of dielectric and/or conductor scatterers, fabricated with printed circuit board (PCB) technology.

The design of an EMMS can be separated into two broad stages: macroscopic and microscopic design steps. Macroscopic design encompasses choosing appropriate surface parameters to realize the desired field transformation. Microscopic design involves realizing these spatially varying surface parameters using meta-atoms with specifically patterned scatterers. Unfortunately, the design processes for both the macroscopic and microscopic design stages are *ad hoc*, time consuming, and cumbersome, as they generally rely on iterative simulations. As a result, there has been some

research into both the macroscopic and microscopic design processes in order to improve them.

There have been many recent efforts to perform macroscopic optimization in a more systematic way. One approach uses an electromagnetic inversion algorithm to solve for the required electric and magnetic surface current densities to produce a desired far-field pattern [3], [4]. This method utilizes the equivalence principle, whereby enforcing Love's condition and local power conservation using a gradient-based method, a passive and lossless EMMS is derived. Upon completion, one arrives at a 3-layer surface admittance profile for an EMMS yielding a far-field pattern with good agreement with a target pattern. One drawback of this method is that it requires that the target far-field pattern be completely defined so that the pattern from the EMMS can be matched to it, rather than imposing application-specific constraints on the far-field. Budhu *et al.* utilize the method of moments (MoM) to model multi-layer EMMSs and subsequently optimize them to achieve desired, fully-specified far-field patterns [5], [6]. This was further extended to dual-band stacked metasurfaces [5]. Similar to the previously described method, this also requires fully defined fields rather than providing the ability to satisfy far-field constraints with a passive and lossless EMMS. In contrast to the two previous approaches, Ataloglou *et al.* explicitly invoke auxiliary fields (AFs) to realize Taylor [7] and uniform [8] aperture distributions. More recently, this method was used to optimize a MoM-based meta-wire structure with an integrated feed for far-field beam forming and MIMO applications [9]. This approach optimizes the AFs by attempting to satisfy a fully specified desired aperture field distribution. The approach requires a fully defined target aperture field and so cannot optimize for loosely defined objectives in its current form. All of these works in their present form require a fully formed target far-field pattern or aperture field. This is slightly disconnected from typical antenna design applications where the designer is given far-field specifications, rather than an exact pattern, to match.

Microscopic optimization conventionally involves choosing a certain meta-atom design with adequate degrees of freedom to arbitrarily manipulate the amplitude and phase of incoming electric field based on its polarization. The meta-atom selection is typically accomplished by conducting iterative simulations of different structures based on empirical methods to converge to a successful candidate. Moreover, the properties of the meta-atoms are derived assuming local periodicity. Therefore, in a quasi-periodic EMMS, to reduce mutual coupling between adjacent meta-atoms, usually one type of structure is selected and the dimension of its scatterers are tuned to realize the desired scattering properties. Non-local design procedures are much less common because they require accurate models of the EMMS as a whole. However, recently, there has been some work to streamline this process.

Inspired by the revolution that data-driven machine learning methods have made in material informatics applied to fields such as quantum materials, pharmaceuticals, and chemistry [10], deep machine learning [11]–[16] and statistical learning [17] methods can help to build surrogate models that can provide fast predictions of the properties of each unit cell. Moreover, several machine learning techniques have been proposed to tackle the challenges of the microscopic design step [18]–[27]. Some of these proposed methods deal with the inverse design of uniform EMMSs, where the impact of inter-cell mutual coupling is less of an issue [18], [19], [22], [23], [28]–[30], while the rest optimize over a simple solution space that is composed of only one scatterer shape [24]–[27]. It is worth noting that dielectric optical EMMSs can be designed using global optimization methods due to the analytical relation between the scatterers' properties and the EMMS's scattering parameters [20]. However, due to the lack of such relations in EMMSs composed of metallic scatterers, the inverse design of a heterogeneous bianisotropic EMMS is more challenging. Nonetheless, solving this problem more efficiently has led to the proposal of systematic approaches that provide both the optimized surface properties and the actual physical unit cells for specific applications [5], [26], [31].

In order to make the EMMS design process more streamlined, we aim to use the integrated macroscopic and microscopic optimizers the authors previously presented [32] to solve for an EMMS that forms two beams. Although the results were previously verified in simulation using Ansys HFSS, we will go one step further to experimentally verify them using a fabricated EMMS illuminated by a standard gain horn (SGH) in a near-field chamber. Importantly, we will also investigate how the macroscopic optimizer utilizes AFs as an extra degree of freedom in its solution.

We will begin by giving a brief overview of the alternating direction method of multipliers (ADMM)-based macroscopic optimizer in Section II. Following this, we will show how the macroscopic optimizer leverages AFs to ensure a passive and lossless design Section III. We will then outline how the microscopic optimizer uses deep-learning neural networks and particle swarm optimization to solve for unit cells in Section IV. We next utilize the macroscopic and microscopic optimization steps to synthesize a two-beam EMMS in Section V. Experimental verification of the optimized two-beam EMMS is shown in Section VI. Lastly, some concluding remarks are offered in Section VII.

II. ADMM-BASED MACROSCOPIC OPTIMIZER

The macroscopic optimizer is similar to the ones reported previously [32], [33]. It is formulated using a homogenized two-dimensional EMMS model constructed with the MoM. This homogenized model captures omega-type bianisotropic behavior of an EMMS. Importantly, the model incorporates the important mutual coupling and edge effects for EMMSs.

The macroscopic model is constructed using the two-dimensional MoM. We first describe the electric and magnetic surface current densities on the EMMS using N pulse basis functions yielding the expansion coefficients $\mathbf{I}^e \in \mathbb{C}^N$ and $\mathbf{I}^m \in \mathbb{C}^N$ respectively. We then use point matching, in conjunction with the incident field across the EMMS, to construct the MoM coupling matrices $[\mathbf{Z}^e] \in \mathbb{C}^{N \times N}$ and $[\mathbf{Z}^m] \in \mathbb{C}^{N \times N}$ respectively. These matrices relate the incident field with the induced surface current densities.

We consider a one-dimensional EMMS located along the y -axis, which is uniform in the x -direction. This configuration is shown in Figure 1. In this paper we will restrict our consideration to TE-polarized examples for a passive, lossless, omega-type bianisotropic EMMS. These surface parameters can be described in a few different ways, but we will use the surface electric impedance (Z_{se}), magnetic admittance (Y_{sm}), and electro-magnetic coupling (K_{em}) representation. For a passive and lossless structure, $\Re\{Z_{se}\} = \Re\{Y_{sm}\} = \Im\{K_{em}\} = 0$. As a result, the surface parameters in the two-dimensional problem reduce to a scalars jX_{se} , jB_{sm} , and K_{em} . This yields the matrix equations [32], [33]

$$\tilde{\mathbf{E}}^{inc} = [\tilde{\mathbf{Z}}_e]\tilde{\mathbf{I}}^e + [\tilde{\mathbf{X}}_{se}]\tilde{\mathbf{I}}^e + [\tilde{\mathbf{K}}_{em}]\tilde{\mathbf{I}}^m \quad (1)$$

$$\tilde{\mathbf{H}}^{inc} = [\tilde{\mathbf{Z}}_m]\tilde{\mathbf{I}}^m + [\tilde{\mathbf{B}}_{sm}]\tilde{\mathbf{I}}^m - [\tilde{\mathbf{K}}_{em}]\tilde{\mathbf{I}}^e, \quad (2)$$

where $\tilde{\mathbf{E}}^{inc}$ and $\tilde{\mathbf{H}}^{inc}$ are the incident electric and magnetic field, $[\tilde{\mathbf{Z}}_e]$ and $[\tilde{\mathbf{Z}}_m]$ are the two MoM matrices for calculating the scattered field, and $\tilde{\mathbf{I}}^e$ and $\tilde{\mathbf{I}}^m$ are the electric and magnetic surface current density coefficients. The $\tilde{\cdot}$ notation denotes the separation of real and imaginary portions of a complex number [33] as optimization with complex numbers adds another layer of complexity. There is no problem information lost when performing this conversion.

Satisfaction of (1) and (2) ensures that the EMMS is passive, lossless, and omega-type bianisotropic *by construction*. Optimizing only the surface current densities for far-field objectives would likely result in an active and/or lossy solution for the surface parameters. As a result, we need to consider both the surface parameters and surface currents when optimizing to ensure that the solution satisfies (1) and (2).

In order to impose constraints on the far-field, we require matrices $[\tilde{\mathbf{G}}^e]$ and $[\tilde{\mathbf{G}}^m]$ to transform the surface current density coefficients to the far-field. As a result, our expression for the total field becomes

$$\tilde{\mathbf{E}}_{ff}^{tot} = [\tilde{\mathbf{G}}^e]\tilde{\mathbf{I}}^e + [\tilde{\mathbf{G}}^m]\tilde{\mathbf{I}}^m + \tilde{\mathbf{E}}_{ff}^{inc} \quad (3)$$

where $\tilde{\mathbf{E}}_{ff}^{inc}$ is the far-field of the incident field's contribution across the extent of the EMMS.

From this, we can construct an optimization program

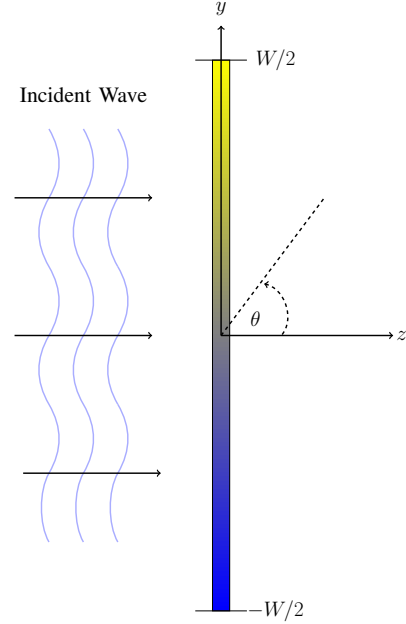


FIGURE 1: The EMMS is finite with width W and coincident with the y -axis, while uniform and infinite in the x -direction.

$$\begin{aligned} & \underset{\substack{\mathbf{I}^e, \mathbf{I}^m, \\ [\mathbf{X}_{se}], [\mathbf{B}_{sm}], [\mathbf{K}_{em}], \\ \gamma_{D^e}, \gamma_{D^m}}}{\text{minimize}} & \alpha_{MB} f_{MB}(MB) + \alpha_{NU} f_{NU}(NU) \\ & + \alpha_D f_D \end{aligned} \quad (4a)$$

$$\begin{aligned} & \text{subject to} & \tilde{\mathbf{E}}^{inc} = [\tilde{\mathbf{Z}}_e]\tilde{\mathbf{I}}^e + [\tilde{\mathbf{X}}_{se}]\tilde{\mathbf{I}}^e + [\tilde{\mathbf{K}}_{em}]\tilde{\mathbf{I}}^m & (4b) \\ & & \tilde{\mathbf{H}}^{inc} = [\tilde{\mathbf{Z}}_m]\tilde{\mathbf{I}}^m + [\tilde{\mathbf{B}}_{sm}]\tilde{\mathbf{I}}^m - [\tilde{\mathbf{K}}_{em}]\tilde{\mathbf{I}}^e & (4c) \end{aligned}$$

$$\begin{aligned} & |[\tilde{\mathbf{G}}^e](SL)\tilde{\mathbf{I}}^e + [\tilde{\mathbf{G}}^m](SL)\tilde{\mathbf{I}}^m \\ & + \tilde{\mathbf{E}}_{ff}^{inc}(SL)| \leq \tau \end{aligned} \quad (4d)$$

$$|[\mathbf{D}]\tilde{\mathbf{I}}^e| = \mathbf{D}_{max}^e + \gamma_{D^e} \quad (4e)$$

$$|[\mathbf{D}]\tilde{\mathbf{I}}^m| = \mathbf{D}_{max}^m + \gamma_{D^m} \quad (4f)$$

$$\mathbf{X}_{se}^{min} \leq \text{diag}([\mathbf{X}_{se}]) \leq \mathbf{X}_{se}^{max} \quad (4g)$$

$$\mathbf{B}_{sm}^{min} \leq \text{diag}([\mathbf{B}_{sm}]) \leq \mathbf{B}_{sm}^{max} \quad (4h)$$

$$\mathbf{K}_{em}^{min} \leq \text{diag}([\mathbf{K}_{em}]) \leq \mathbf{K}_{em}^{max}. \quad (4i)$$

The optimization variables in this case are the surface electric and magnetic current densities ($\mathbf{I}^e, \mathbf{I}^m$), the passive and lossless surface parameters ($[\mathbf{X}_{se}], [\mathbf{B}_{sm}], [\mathbf{K}_{em}]$), and the slack variables ($\gamma_{D^e}, \gamma_{D^m}$). The side lobe level τ , over specified angles SL , is constrained in (4d). The second derivative of the surface current densities are constrained with (4e) and (4f) in order to aid numerical stability. The limits of the achievable surface parameters are also constrained in (4g), (4h), and (4i) with predefined limits \mathbf{X}_{se}^{min} , \mathbf{X}_{se}^{max} , \mathbf{B}_{sm}^{min} , \mathbf{B}_{sm}^{max} , \mathbf{K}_{em}^{min} , and \mathbf{K}_{em}^{max} . The terms α_{MB} , α_{NU} , and α_D are the hyper-parameters, which can be used to weight the relative values of the components of the objective

function to aid convergence. The function

$$f_{MB}(MB) = \|\tilde{\mathbf{G}}^e(MB)\tilde{\mathbf{I}}^e + [\tilde{\mathbf{G}}^m](MB)\tilde{\mathbf{I}}^m + \tilde{\mathbf{E}}_{ff}^{inc}(MB) - MB_{level}\|_2^2 \quad (5)$$

aims to match the field level at an angle MB to a desired field level MB_{level} . Similarly, the function

$$f_{NU}(NU) = \|\tilde{\mathbf{G}}^e(NU)\tilde{\mathbf{I}}^e + [\tilde{\mathbf{G}}^m](NU)\tilde{\mathbf{I}}^m + \tilde{\mathbf{E}}_{ff}^{inc}(NU)\|_2^2 \quad (6)$$

simply aims to minimize the field at an angle NU , thereby producing a null in the far-field pattern there. Lastly, the function

$$f_D = \|(\gamma_{D^e})_+\|_2^2 + \|(\gamma_{D^m})_+\|_2^2, \quad (7)$$

where $(\cdot)_+$ returns the value of the input if it is positive and zero for negative inputs, minimizes the positive values of the slack variables γ_{D^e} and γ_{D^m} . As a result, this function aims to minimize the amount of curvature in the current densities that exceeds the user-defined values \mathbf{D}_{max}^e and \mathbf{D}_{max}^m . Using slack variables for (4e) and (4f) allows for some violation of the constraint during optimization to aid convergence.

This model contains non-convex bilinear terms in (4b) and (4c), which cannot be optimized with fast and efficient convex solvers. To circumvent this, we use a non-linear optimization technique called the alternating direction method of multipliers (ADMM). The algorithm first forms the augmented Lagrangian, transferring the equality constraints in (4b) and (4c) to the objective. The two equality constraints are combined into a single function f_Z and added to the objective as

$$f_{Z_e} = \frac{\rho}{2} \|\tilde{\mathbf{E}}^{inc} + [\tilde{\mathbf{Z}}_e]\tilde{\mathbf{I}}^e + [\tilde{\mathbf{X}}_{se}]\tilde{\mathbf{I}}^e + [\tilde{\mathbf{K}}_{em}]\tilde{\mathbf{I}}^m\|_2^2 + \boldsymbol{\mu}_{Z_e}^T \left(-\tilde{\mathbf{E}}^{inc} + [\tilde{\mathbf{Z}}_e]\tilde{\mathbf{I}}^e + [\tilde{\mathbf{X}}_{se}]\tilde{\mathbf{I}}^e + [\tilde{\mathbf{K}}_{em}]\tilde{\mathbf{I}}^m \right) \quad (8)$$

$$f_{Z_m} = \frac{\rho}{2} \|\tilde{\mathbf{H}}^{inc} + [\tilde{\mathbf{Z}}_m]\tilde{\mathbf{I}}^m + [\tilde{\mathbf{B}}_{sm}]\tilde{\mathbf{I}}^m - [\tilde{\mathbf{K}}_{em}]\tilde{\mathbf{I}}^e\|_2^2 + \boldsymbol{\mu}_{Z_m}^T \left(-\tilde{\mathbf{H}}^{inc} + [\tilde{\mathbf{Z}}_m]\tilde{\mathbf{I}}^m + [\tilde{\mathbf{B}}_{sm}]\tilde{\mathbf{I}}^m - [\tilde{\mathbf{K}}_{em}]\tilde{\mathbf{I}}^e \right) \quad (9)$$

$$f_z = f_{Z_e} + \beta f_{Z_m} \quad (10)$$

where f_Z is a weighted sum of the two functions f_{Z_e} and f_{Z_m} , ρ is a user-defined penalty parameter, β is a real number used to scale f_{Z_m} , and $\boldsymbol{\mu}_{Z_e}$ and $\boldsymbol{\mu}_{Z_m}$ are dual variables. The dual variables are updated each iteration i according to

$$\boldsymbol{\mu}_{Z_e}^{i+1} = \boldsymbol{\mu}_{Z_e}^i + \rho \left(-\tilde{\mathbf{E}}^{inc} + [\tilde{\mathbf{Z}}_e]\tilde{\mathbf{I}}^e + [\tilde{\mathbf{X}}_{se}]\tilde{\mathbf{I}}^e + [\tilde{\mathbf{K}}_{em}]\tilde{\mathbf{I}}^m \right) \quad (11)$$

$$\boldsymbol{\mu}_{Z_m}^{i+1} = \boldsymbol{\mu}_{Z_m}^i + \rho \left(-\tilde{\mathbf{H}}^{inc} + [\tilde{\mathbf{Z}}_m]\tilde{\mathbf{I}}^m + [\tilde{\mathbf{B}}_{sm}]\tilde{\mathbf{I}}^m - [\tilde{\mathbf{K}}_{em}]\tilde{\mathbf{I}}^e \right). \quad (12)$$

This new optimization program has the form

$$\begin{aligned} & \underset{\substack{\mathbf{I}^e, \mathbf{I}^m \\ [\mathbf{X}_{se}], [\mathbf{B}_{sm}], [\mathbf{K}_{em}], \\ \gamma_{D^e}, \gamma_{D^m}}}{\text{minimize}} & \alpha_{MB} f_{MB}(MB) + \alpha_{NU} f_{NU}(NU) \\ & + \alpha_D f_D + f_Z \end{aligned} \quad (13a)$$

$$\text{subject to} \quad \|\tilde{\mathbf{G}}^e(SL)\tilde{\mathbf{I}}^e + [\tilde{\mathbf{G}}^m](SL)\tilde{\mathbf{I}}^m + \tilde{\mathbf{E}}_{ff}^{inc}(SL)\| \leq \tau \quad (13b)$$

$$\|[\mathbf{D}]\tilde{\mathbf{I}}^e\| = \mathbf{D}_{max}^e + \gamma_{D^e} \quad (13c)$$

$$\|[\mathbf{D}]\tilde{\mathbf{I}}^m\| = \mathbf{D}_{max}^m + \gamma_{D^m} \quad (13d)$$

$$\mathbf{X}_{se}^{min} \leq \text{diag}([\mathbf{X}_{se}]) \leq \mathbf{X}_{se}^{max} \quad (13e)$$

$$\mathbf{B}_{sm}^{min} \leq \text{diag}([\mathbf{B}_{sm}]) \leq \mathbf{B}_{sm}^{max} \quad (13f)$$

$$\mathbf{K}_{em}^{min} \leq \text{diag}([\mathbf{K}_{em}]) \leq \mathbf{K}_{em}^{max}. \quad (13g)$$

ADMM optimizes (13) for the surface electric and magnetic current densities and then surface parameters with each iteration. This has the effect of breaking the original non-convex problem into smaller, convex ones. Solutions which satisfy the desired problem specifications can usually be found in roughly one hundred iterations.

III. LEVERAGING AUXILIARY FIELDS TO ENSURE SATISFACTIONS OF GSTCS

In previous work by Epstein *et al.* [34], it is shown that leveraging the AFs introduced on either side of a metasurface can help satisfy local power conservation. This allows for arbitrary field transformations with passive and lossless omega-type bianisotropic surfaces. These AFs are evanescent and as a result, do not contribute to the far-field pattern of interest. Recently, work has been done to optimize these AFs to tailor aperture fields for beamforming [7] along with Chebyshev and Taylor array patterns [35]. In contrast, the macroscopic optimizer outlined in Section II does not directly optimize the AFs to achieve these transformations with a passive and lossless omega-type bianisotropic surface. The macroscopic optimizer instead indirectly leverages AFs to satisfy the passive and lossless GSTCs equality constraints through jointly optimizing the surface currents and parameters. To show that the optimizer is indeed leveraging AFs, we will first decompose the surface current densities into their radiating and the non-radiating components used to satisfy the GSTCs [36]. We will then show an example of extreme angle reflection and compare it to an analytically derived solution, which requires AFs [34].

A. SEPARATING RADIATING AND NON-RADIATING CURRENT CONTRIBUTIONS

The surface current densities contain both a radiating component, which is detectable in the far-field, and a non-radiating component, which is evanescent. Salucci *et al.* [36] illustrate that singular value decomposition (SVD) can be performed on the far-field transformation matrices $[\mathbf{G}^e]$ and $[\mathbf{G}^m]$, shown in (3), to find the most significant current components contributing to the far-field pattern. To perform this, we calculate the scattered field from surface electric and

magnetic current densities and then perform SVD as

$$\mathbf{E}_{ff}^e + \mathbf{E}_{ff}^m = [\mathbf{G}^e \ \mathbf{G}^m] \begin{bmatrix} \mathbf{I}^e \\ \mathbf{I}^m \end{bmatrix} \quad (14a)$$

$$\mathbf{E}_{ff}^{scat} = \mathbf{G}\mathbf{I}, \quad (14b)$$

$$\mathbf{E}_{ff}^{scat} = \mathbf{U}\Sigma\mathbf{V}^H\mathbf{I}, \quad (14c)$$

where H is the complex conjugate transpose. If we take the most significant singular values, defined by a variable ξ , contributing to this radiated field, we can find the radiating surface current densities (\mathbf{I}_{rad}) as

$$\mathbf{I}_{rad} = \mathbf{V}_\xi \Sigma_\xi^{-1} \mathbf{U}_\xi^H \mathbf{E}_{ff}^{scat} \quad (15)$$

These components are termed ‘‘radiating’’, while the remaining currents (i.e. the currents corresponding to the less significant singular values) are ‘‘non-radiating’’. The \cdot_ξ notation signifies the truncated SVD matrices. These non-radiating currents can be associated with the evanescent AFs. When removed, the far-field radiation pattern remains essentially unchanged. While Salucci *et al.* use non-radiating currents for various purposes, e.g. to impose forbidden regions for currents, we use them as degrees of freedom to achieve the required passivity and losslessness imposed by (1) and (2). Indeed, it is shown that these additional degrees of freedom are required for some wave transformations, such as perfect reflection and transmission, which redistribute power across the EMMS [34].

B. EXAMPLE OF EXTREME ANGLE REFLECTION EMMS REQUIRING AUXILIARY FIELDS

Epstein *et al.* [34] demonstrate that AFs are required to perform perfect reflection from an incident plane wave on an infinite metasurface. Our MoM model is finite, which is not accounted for in the example by Epstein *et al.* Nevertheless, introducing AFs significantly improves the performance. Here we aim to achieve similar performance to their perfect reflection far-field pattern using the macroscopic optimizer to show that the optimizer leverages AFs. We will then evaluate the near field spectrum and use SVD to verify the extent to which AFs are used to satisfy the GSTCs. We attempt perfect reflection to $\theta = 108^\circ$ from an incident plane wave at $\theta = 0^\circ$ for the EMMS shown in Figure 1.

1) PROBLEM FORMULATION

In order to perform extreme angle reflection, we must supply a set of far-field goals for the optimizer described in Section II to attempt to satisfy. Because our task is simply to form a beam at $\theta = 108^\circ$, our only far-field criteria will be to match the total radiated field to a predetermined value (MB_{level}) at that angle. In order to maintain numerical stability, we will also impose constraints on the maximum allowable curvature of the electric (\mathbf{D}_{max}^e) and magnetic surface current densities (\mathbf{D}_{max}^m). The full list of optimization parameters is shown in Table 1.

TABLE 1: Extreme-angle reflection optimization parameters

	Value
Surface Width (W)	$6\lambda_0$
Incident Field (E^{inc})	$e^{-jkz}\hat{x}$ [V/m] uniform along the EMMS
Angular Sampling Points (M)	361
Spatial Sampling Points (N)	300
Max Iterations	100
Initial Conditions	$([\tilde{\mathbf{X}}_{se}]^0, [\tilde{\mathbf{B}}_{sm}]^0, [\tilde{\mathbf{K}}_{em}]^0) = \mathbf{0}$, $\rho = 10, \beta = 1000, (\mu_{Le}^0, \mu_{Lm}^0) = \mathbf{0}$
$\{\alpha_{MB}, \alpha_{NU}, \alpha_{DE}, \alpha_{DH}\}$	$\{150, 0, 5, 1\}$
Main Lobe Angle (MB)	$\theta = 108^\circ$
Main Lobe Level (MB_{level})	6 [V/m]
$\{\mathbf{D}_{max}^e, \mathbf{D}_{max}^m\}$	$\{\mathbf{0.5}, \mathbf{225}\}$

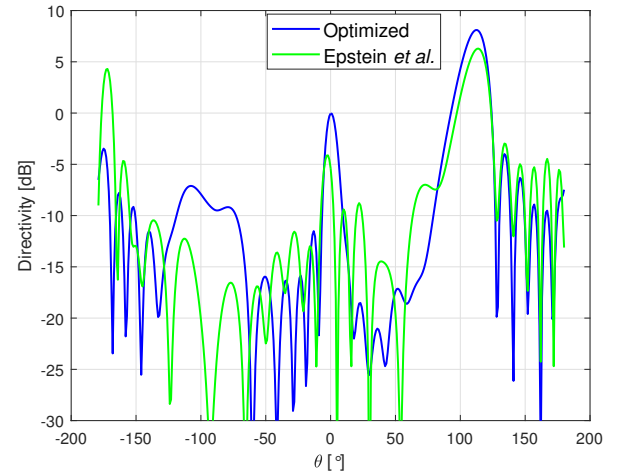
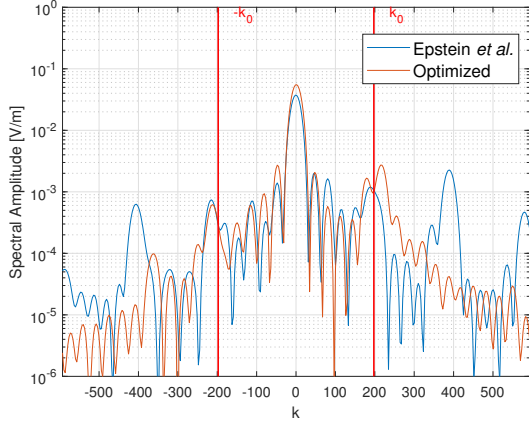


FIGURE 2: Directivity of extreme angle reflection towards $\theta = 108^\circ$ from an incident uniform illumination at $\theta = 0^\circ$. The optimized results are from the ADMM-based optimizer and analytical results are from Epstein *et al.* [34] using AFs.

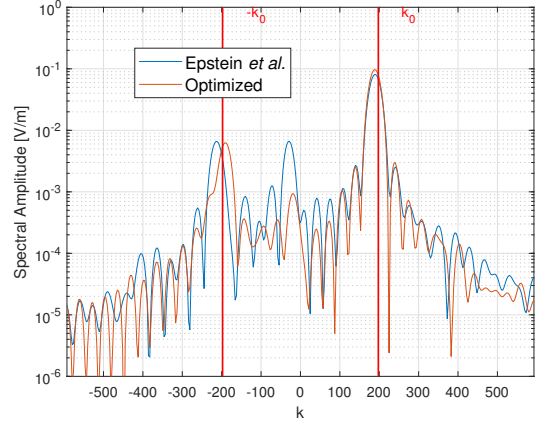
2) RESULTS

After optimizing the surface parameters with the program described in Section 1, we arrive at the far-field pattern shown in Figure 2. We have also shown in the far-field results of an analytical formulation derived by Epstein *et al.* [34], which uses AFs to perform perfect extreme angle reflection for an infinite surface.

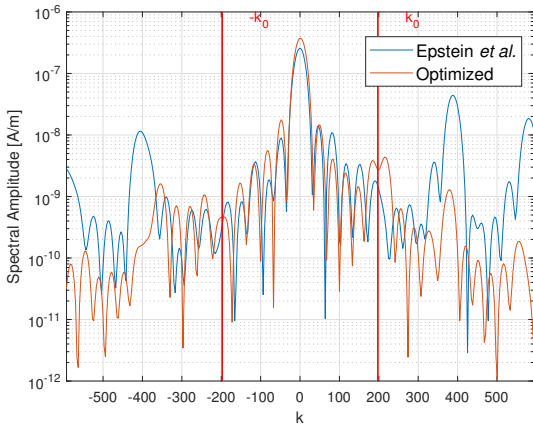
The analytical formulation will not exhibit perfect reflection because the surface parameters were derived assuming an infinite surface, while the surface considered is only $6\lambda_0$ long. This is evident from the spurious lobes apparent in the far-field directivity plot in Figure 2. The optimized far-field has slightly greater directivity compared to the analytic formulation. The improved directivity suggests that the optimizer factors in the finite width of the surface and adjusts the generation of the AFs to satisfy the far-field goals.



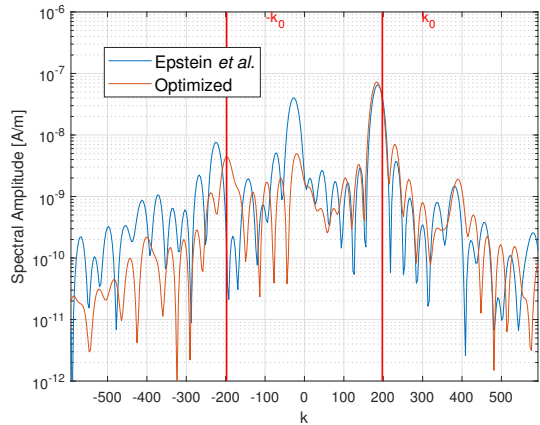
(a) Electric field spectrum for $z > 0$



(a) Electric field spectrum for $z < 0$



(b) Magnetic field spectrum for $z > 0$



(b) Magnetic field spectrum for $z < 0$

FIGURE 3: Electric (a) and magnetic (b) field spectra for $z > 0$ (on the transmitted side of the EMMS)

FIGURE 4: Electric and magnetic field spectra for $z < 0$ (on the reflected side of the EMMS)

In order to verify the extent to which AFs are leveraged, we examine the spectrum of the electric and magnetic fields just above and below the surface. We compare the analytic spectrum with the optimized one on top of and below the EMMS in Figure 3 and Figure 4 respectively. As expected, the analytic formulation, which explicitly excites AFs, has the expected peak in spectrum around $k = \pm 2k_0$, in order to perform the transformation [34]. The optimized solution does not have the same obvious peak, however there is still an increased level of non-radiating spectrum with $k > |k_0|$. The differences are attributed to the finite nature of the EMMS, which requires different AFs to satisfy the problem goals than an infinite one.

We can further investigate the existence of AFs by examining the time-averaged power density redistributed above and below the EMMS. To do this, we calculate the near fields from our optimized surface currents in COMSOL. The time averaged power density can be seen in Figure 5 above

and below the EMMS along with the analytically-predicted power profile by Epstein *et al.* It is clear from analyzing the time-averaged power density at the input side of the surface that there is seemingly active/lossy behaviour without explicitly invoking the use of AFs with our passive/lossless EMMS. Interestingly, the spatial frequency of the power density profile matches relatively well between the input side of the EMMS and the analytically predicted result. Due to this example not achieving perfect reflection, there is naturally some time-averaged power density on the transmitted side of the EMMS ($z > 0$).

Lastly, we can quantify the extent that AFs are used if we isolate the non-radiating currents and remove them from the MoM matrix equations. Satisfaction of these MoM matrix equations is critical for maintaining a passive and lossless solution per their construction. Removing the non-radiating surface currents requires an active and lossy EMMS because the MoM equality constraints, (4b) and (4c), are no longer

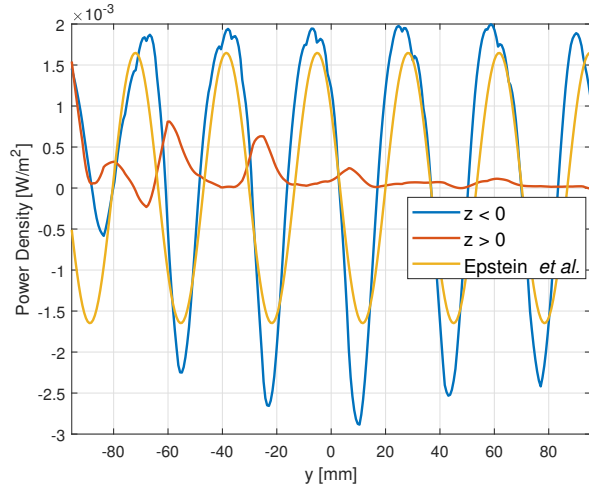


FIGURE 5: Time averaged power density above and below the EMMS. The analytical results are from Epstein *et al.* using AFs and arbitrary phase shift $\xi_{out} = 288^\circ$. [34]

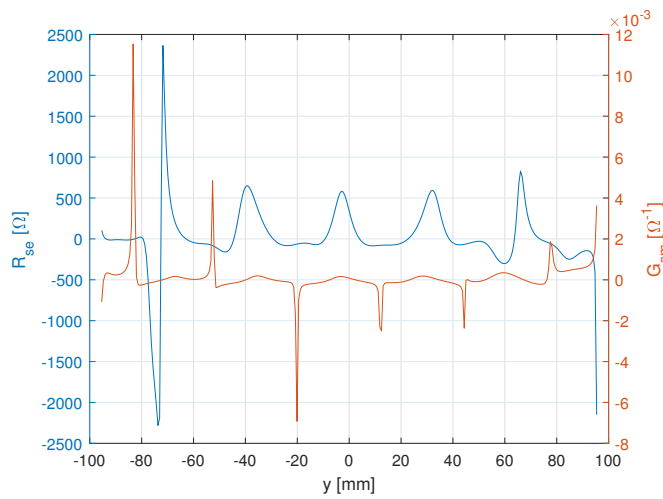


FIGURE 6: Active and lossy components of Z_{se} and Y_{sm} (R_{se} and G_{sm} respectively) required to satisfy the MoM equality constraints for the extreme reflection example if the non-radiating portion of the surface current densities are removed.

satisfied for these new, purely radiating surface current densities. For this extreme reflection example, the non-negligible active and lossy components of the surface electric impedance and magnetic admittance are shown in Figure 6. The two curves clearly show non-negligible real parts in the surface impedances and admittances. The bianisotropic coupling becomes a redundant degree of freedom with an active and lossy EMMS, so it is not shown. As expected, the non-radiating spectrum of the surface current densities chosen by the optimizer play a vital role in performing passive and lossless field transformations.

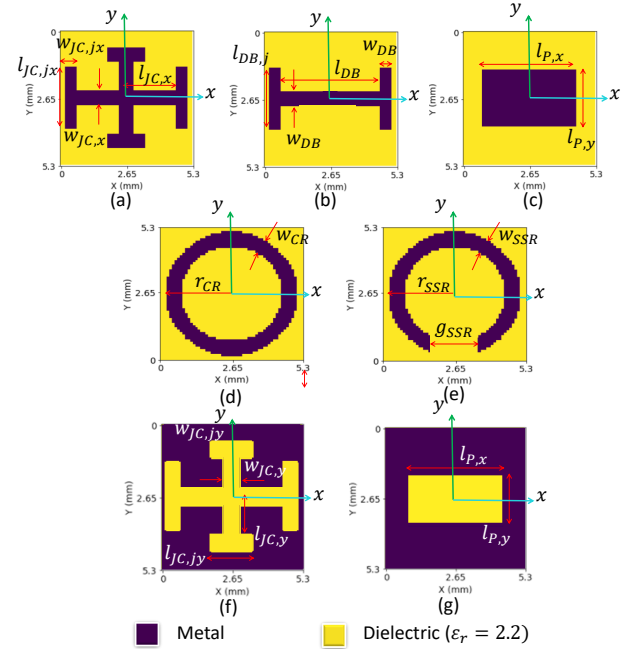


FIGURE 7: Primitives used to generate three-layer bianisotropic unit cells: (a)-(e) possible capacitive primitives on all the layers, and (f)-(g) additional inductive primitives on the middle layer.

IV. MICROSCOPIC OPTIMIZER USING DNN SURROGATE MODELS

In the microscopic design step, the optimized set of (Z_{se}, Y_{sm}, K_{em}) are first converted to scattering parameters and then are realized using physical unit cells. To find the optimized unit cell, a previously proposed approach is employed [32].

First, about 70,000 three-layer bianisotropic unit cells with a period of 5.3 mm and composed of the primitives shown in Figure 7 are simulated using an accelerated in-house periodic MoM tool between 1.0 and 19.0 GHz. The scatterers on the top and bottom layers can be any of the primitives in Figure 7 (a)-(e) while the scatterer on the middle layer can be any of the primitives in Figure 7 (a)-(g). The scatterers are separated using RT Duroid 5880 ($\epsilon_r = 2.2$) with a standard thickness in $\{0.254, 0.508, 0.787, 1.524\}$ mm. Once these unit cells are simulated, their scattering parameters (S-parameters) for normal incidence of transverse electric (TE) and transverse magnetic (TM) fields are stored.

To predict the S-parameters of the unit cells composed of new combinations of the shown primitives, we train two deep-learning neural networks (DNNs) comprising fully-connected layers of neurons as surrogate models. These networks are specifically adept at extracting the underlying features in large data sets and predicting their properties accurately. This is particularly useful in the case of thin EMMSs, where the inter-layer coupling between the scatterers of each unit cell is non-negligible. Therefore, in thin

unit cells, interpolation of properties based on dimensions of the scatterers will likely cause inaccuracy in the predicted S-parameters.

The two DNNs, *mag*-DNN and *phase*-DNN, are used to predict the magnitude and phase of the S-parameters, respectively. Both of them accept the frequency of interest and a *feature* variable as the inputs. Here, the *feature* variable represents the physical structure of the unit cell including the category of the constituent scatterers, (shown in Figure 7), the dimensions of the scatterers, and the thickness of the substrate. The feature variable for each unit cell is composed of total of 30 binary and continuous values. The binary values are used for the shape of the primitive and the standard thickness of the substrate, while the continuous values specify dimensions of features unique to each scatterer. The *mag*-DNN simultaneously predicts the transmission and reflection coefficients of the TE and TM fields under normal incidence as four outputs. However, to predict the phase of each of these parameters, a separate DNN is trained for each. Moreover, each *phase*-DNN receives one more additional input: the magnitude of the corresponding S-parameters at a certain frequency. Adding the magnitude of the S-parameter improves the accuracy of the DNN in predicting the phase response at the resonance frequencies. A *phase*-DNN outputs three parameters that can be used to calculate the absolute phase of each unit cell [32].

The *mag*- and *phase*-DNNs are composed of 6 hidden layers with N_{H1} , N_{H2} , N_{H3} , N_{H3} , N_{H2} , N_{H1} neurons, respectively from the shallowest layer to the deepest layer of the neural networks, as shown in Figure 8. The number of neurons for the *mag*-DNN are $N_{H1} = 100$, $N_{H2} = 500$, and $N_{H3} = 1000$ that end with 4 output neurons with sigmoid activation function. The *phase*-DNN is composed of more neurons, where $N_{H1} = 100$, $N_{H2} = 500$, and $N_{H3} = 2000$. The neural networks are trained using the ADAM optimizer [37] and backpropagation method [38] on 85% of the training set and tested on the remaining 15%. The training is performed for 100 epochs with *early stopping* set to become activated if no improvement in the accuracy is achieved after 10 epochs.

The two DNNs are then integrated in a particle swarm optimization (PSO) utilizing the surrogate models to evaluate the performance of a unit cell under test. For better convergence, the PSO is performed in the 30-dimensional *feature* space of the unit cells. At each iteration, for a certain particle in the swarm, the 30-dimensional feature along with the frequency point of interest is first input to the *mag*-DNN to predict the amplitude of the S-parameters, $|S_{ij}|$. Then, the frequency point, the 30-dimensional feature, and the predicted $|S_{ij}|$, is fed to the *phase*-DNN to predict the phase of the S-parameters. These predicted S-parameters are then compared to the required ones obtained from the macro-optimization design step to see if they meet the requirements. The process described is repeated for the unique obtained sets of the (Z_{se}, Y_{sm}, K_{em}) from the macroscopic design

TABLE 2: Optimization parameters for the two-beam EMMS example

	Value
Wavelength (λ)	31.8 mm
Surface Width (W)	12.67λ
Incident Field (E^{inc})	15 dBi Horn Antenna
Angular Sampling Points (M)	361
Spatial Sampling Points (N)	76
Max Iterations	150
Initial Conditions	$([\tilde{\mathbf{X}}_{se}]^0, [\tilde{\mathbf{B}}_{sm}]^0, [\tilde{\mathbf{K}}_{em}]^0) = \mathbf{0}$, $\rho = 200, \beta = 377, (\mu_{ze}^0, \mu_{zm}^0) = \mathbf{0}$
$\{\alpha_{MB}, \alpha_{NU}, \alpha_{DE}, \alpha_{DH}\}$	$\{500, 500, 400, 1\}$
Main Lobe Angles (MB)	$\theta = \{-20^\circ, 30^\circ\}$
Main Lobe Level (MB_{level})	2.65 [V/m]
Sidelobe Level (τ) and Angles (SL)	$\{-12\text{dB}, -90^\circ \leq \theta \leq -28^\circ\}$, $\{-12\text{dB}, -12^\circ \leq \theta \leq 21^\circ\}$, $\{-12\text{dB}, 39^\circ \leq \theta \leq 90^\circ\}$, $\{-20\text{dB}, 90^\circ \leq \theta \leq 180^\circ\}$, $\{-20\text{dB}, -180^\circ \leq \theta \leq -90^\circ\}$,
Null Angles (NU)	$\theta = \{0^\circ, 180^\circ\}$
$\{\mathbf{D}_{max}^e, \mathbf{D}_{max}^m\}$	$\{\mathbf{0.01}, \mathbf{1}\}$

step to realize the whole EMMS with corresponding physical unit cells.

V. DESIGN EXAMPLE: A BEAM-SPLITTING EMMS

Following the design process described, a one-dimensional $12.67\lambda_0$ (403 mm)-long metasurface varying along the y -direction is designed to radiate two beams at $\theta = -20^\circ$ and $\theta = +30^\circ$. The EMMS is uniform along the x -direction and the beam collimation occurs only in the yz -plane. This surface is composed of 76 unique meta-atoms with a periodicity of 5.3 mm = $\lambda/6$, where $\lambda = 31.8$ mm at 9.4 GHz. Using the incident field produced by a realistic feed, a horn antenna, the optimization problem constraints are listed in Table 2. The feed antenna is modelled after a 3D X-band horn antenna discussed later by slicing it in the H-plane to mimic what will happen in the 3D experiment. The feed is placed 330 mm away from the center of the EMMS. In this configuration, the maximum angle of incidence at the edge of the EMMS is 31.4° . The simulation setup of the uniform EMMS being excited by a slice of the horn antenna is shown in Figure 9.

It is worth noting that the AFs are essential for this optimization problem, because if we remove the non-radiating currents from the homogenized model, the EMMS is required to be active and lossy with real surface electric impedance and magnetic admittance. These active and lossy surface parameters are pictured in Figure 10.

The comparison between the amplitude and phase of the tangential electric field component on the transmitting side of the optimized homogenized model and the physical

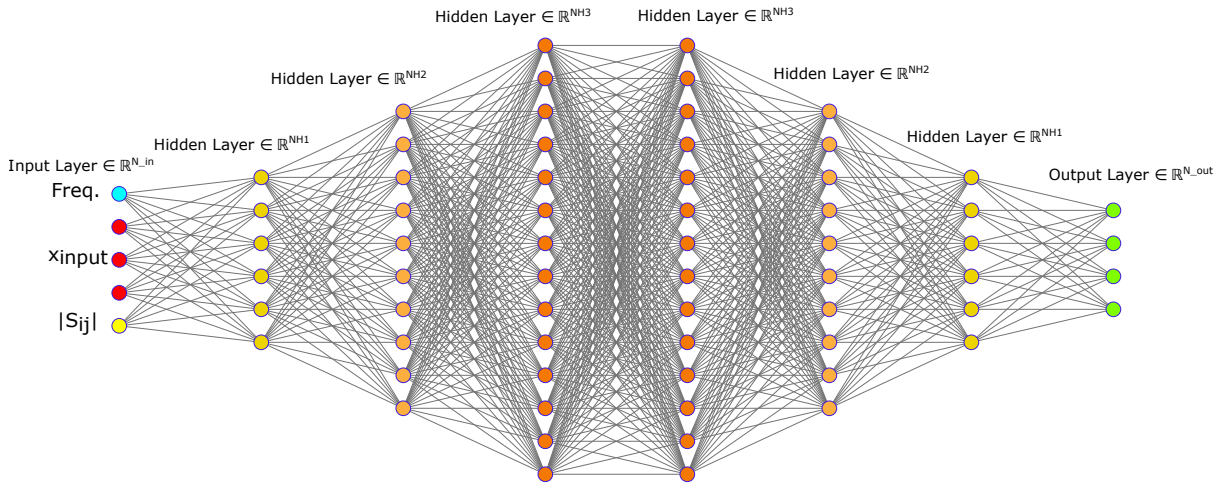


FIGURE 8: Representative architecture of the fully-connected neural networks used to predict the magnitude and phase of the scattering parameters of bianisotropic unit cells. The input node $|S_{ij}|$ is only connected in the *phase-NN*.

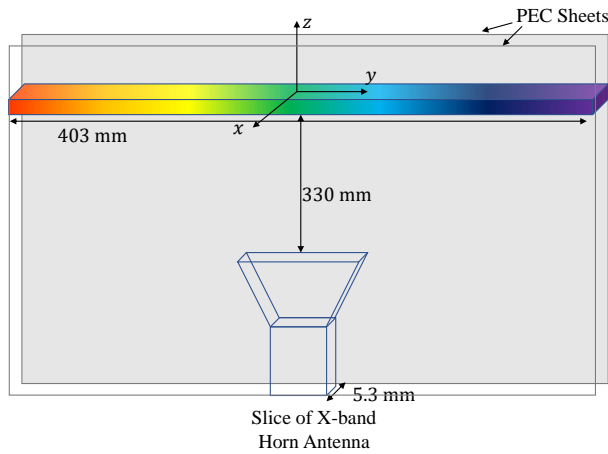


FIGURE 9: Simulation setup of the EMMS that is uniform in x -direction. The EMMS is uniformly excited by a slice of the horn antenna. Both are placed in a parallel plate waveguide between two perfect electric conductors.

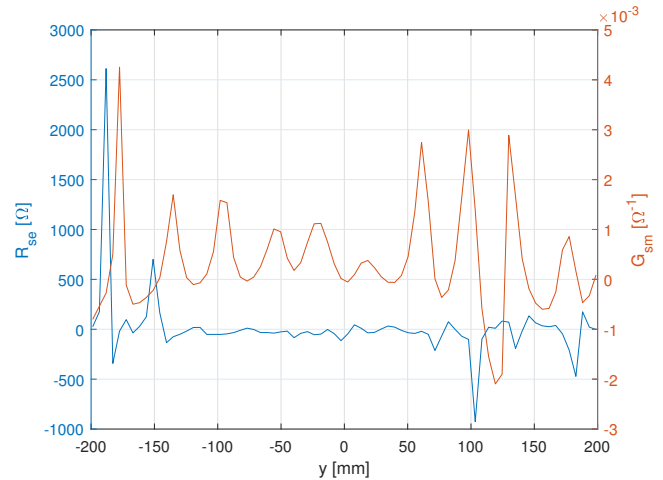


FIGURE 10: Required active and lossy surface parameters if AFs are removed for the two-beam EMMS example.

EMMS is shown in Figure 11. There is good agreement between the desired phases of the homogenized model and the physical unit cells. The amplitude is also well matched for the most part, except at two points. Matching the desired amplitude at $y = 0$ and at $y = 77.9$ mm requires realizing completely inductive surface impedances, i.e. $\Im\{Z_{se}\} > 0$ while $\Im\{Y_{sm}\} = \Re\{K_{em}\} = 0$, by the meta-atom. Since the possible generated meta-atoms in the macroscopic design step have complementary-shaped scatterers in the middle layer but not the top and bottom layers, this may have made it difficult to achieve the required impedances here.

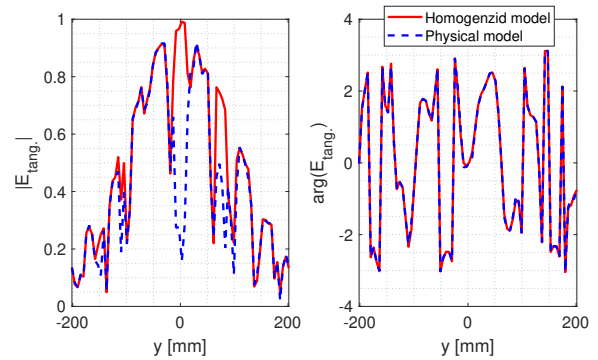


FIGURE 11: Comparison between the amplitude and phase of the tangential components of the transmitted electric field from the EMMS with the optimized macroscopic and microscopic surface properties at 9.4 GHz.

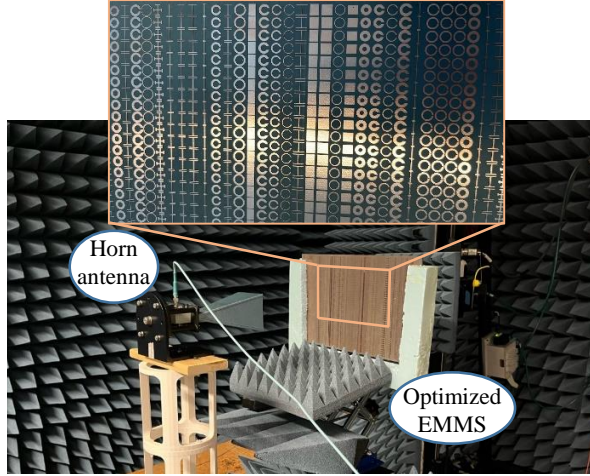
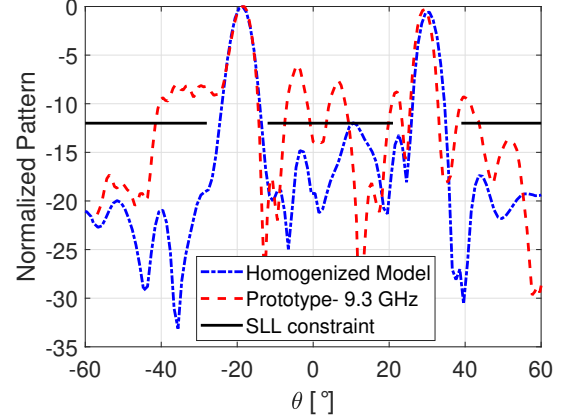
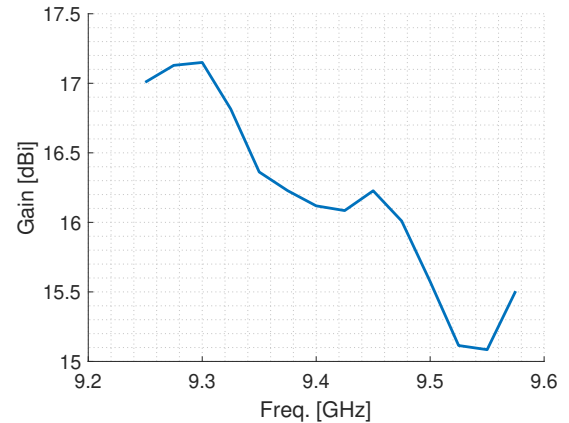


FIGURE 12: The prototype in the measurement setup.

VI. EXPERIMENTAL VALIDATION OF SYNTHESIS METHOD

A prototype of the optimized bianisotropic metasurface with the width of 402.8 mm and length of 243.8 mm is fabricated and tested in a planar near-field antenna scanner using the setup shown in Figure 12. Like the simulation model, this surface has 76 unique meta-atoms varying along the width in the y -direction but is uniform in the x -direction. There are 46 unit cells in the x -direction. A detailed picture of the prototype in this setup is shown in the inset of Figure 12, where it can be seen that the designed EMMS is composed of meta-atoms with many different scatterer shapes.

The normalized radiation patterns of the homogenized model and the prototype are shown in Figure 13, where both patterns have two beams directed at $\theta = -20^\circ$ and $\theta = +30^\circ$. The SLL of the homogenized model's pattern complies with the specified maximum level of -12 dB, whereas the prototype's SLLs are slightly higher than -10 dB. The higher SLLs in the prototype can be attributed to two factors. The first one is the difference between the optimized macroscopic properties and the ones realized by the physical meta-atoms. This occurs when the required surface properties cannot be completely realized by one of the meta-atoms in the considered three-layer solution space. For the example here, one could explore an augmented space that includes inductive scatterers similar to Figure 7 (f)-(g) on all three layers. The second is that although mutual coupling is accounted for in the macroscopic optimization stage, the unit cells for the microscopic optimization stage are optimized for in a periodic environment. This assumption is valid if the unit cells are not changing drastically spatially, which there is not guarantee of in this case. It is worth noting that since the maximum angle of incidence on the EMMS is 31.4° , the performance of the constituent meta-atoms under oblique incidence including and up to 31.4° is stable and close to its properties under normal incidence.

FIGURE 13: Normalized pattern of the homogenized model at 9.4 GHz and the prototype at 9.3 GHz in xz -plane ($\varphi = 0^\circ$) plane.FIGURE 14: Gain of the fabricated EMMS at $\theta = -20^\circ$ and $\varphi = 0^\circ$.

In order to quantify the gain of the surface, we compared the field levels to that of a standard X-band gain horn over the frequencies from 9.2 GHz to 9.5 GHz. The gain of the horn antenna with the prototype in front of it at $\theta = -20^\circ$ is shown in Figure 14 as a function of frequency. The maximum gain is found to be 17.2 dBi at 9.3 GHz. In order to determine the merit of this gain figure compared to the theoretical maximum, we itemize the factors that reduce the realized gain at $\theta = -20^\circ$ in Table 3.

An ideal uniformly illuminated surface with the same length and width of our prototype radiates a pencil beam with a directivity of 30.7 dBi. In our design, this is reduced 5.8 dB by the fact that the EMMS only collimates in the xy -plane. Furthermore, the taper and spillover loss for the planar rectangular EMMS are calculated [39] and amount to 1.4 dB. In addition, since the beam is being split into two directions, the gain is reduced by approximately 3.0 dB. Scanning the beams to -20° and $+30^\circ$ results

TABLE 3: Loss Analysis of the Prototype at $\theta = -20^\circ$

	Value [dB]
Directivity of uniform surface with $W = 12.67\lambda$ & $L = 7.83\lambda$	30.7
Loss due to collimation only in the azimuth direction	5.8
Taper loss	0.9
Spillover loss	0.5
Beam splitting	3.0
Scanning loss	0.3
Transmission Loss of HFSS Model with PEC traces	1.3
Ohmic losses	0.7
Calculated gain	18.2 dBi
Measured gain	17.2 dBi

in minimum of $10 \log_{10}[\cos(-20)^\circ] = 0.3$ dB scanning loss. Furthermore, the HFSS model yields a transmission efficiency of 74.5%, which results in 1.3 dB of transmission loss including the dielectric loss. This transmission efficiency is calculated by comparing the feed's power alone and the power of the feed plus the EMMS composed of perfect electric sheet scatterers on a line on top of the EMMS. Lastly, there is 0.7 dB of ohmic losses from the synthesized meta-atoms comprising scatterers of 0.018 mm-thick copper. To calculate the ohmic losses, first, the meta-atoms composed of copper scatterers under oblique incidence based on their position were simulated with periodic boundary conditions and their scattering parameters were extracted and compared to the case where perfect conductors are used. All of these factors lead to the 18.2 dBi of expected gain from the prototype. With these considerations, there is only 1.0 dB of discrepancy between the predicted and actual measured gain, which is within an acceptable range. The discrepancy can be attributed to manufacturing differences between the HFSS model and the prototype. In addition, there are also some inevitable small phase errors introduced by inaccuracies in the measurement setup.

VII. CONCLUSION

In this paper we have both determined the extent to which our previously reported EMMS optimizer leverages AFs and experimentally verified our EMMS inverse design scheme. The use of AFs was analyzed by performing a challenging extreme-angle reflection to 108° . We then qualitatively evaluated the presence of AFs by examining the near field radiating and evanescent spectrum. To further quantify the existence of AFs, we used SVD to isolate the non-radiating spectrum and evaluate its importance in satisfying the passive and lossless GSTCs. Both methods reveal that AFs are vital as a degree of freedom for the macroscopic optimizer to perform the field transformations studied.

We then used this method to design an EMMS based on far-field goal in the form of two equal beams at $\theta = -20^\circ$ and 30° with a side lobe level of -12 and -20 dB. These

surface parameters were fed into the machine learning-based microscopic optimizer to design a set of physical meta-atoms. These meta-atoms were obtained without the need for heuristically tuning constituent scatterer geometries. This surface was then fabricated and evaluated in an experimental measurement. The prototype's far-field pattern matches well with the original main beam direction and side lobe specifications.

This end-to-end methodology yields good results without the designer needing to iteratively tune meta-atom physical properties. Furthermore, we have been able to experimentally verify the results with good agreement with a theoretical maximum gain. However, there are some areas to improve upon this promising EMMS design method. Firstly, the macroscopic optimizer is still configured for a two-dimensional EMMS. Moving to three dimensions will allow for more sophisticated beam forming and collimation in the elevation plane. Secondly, adding a minimum gain mask to the macroscopic design step will allow for specification of more sophisticated design goals such as isoflux and cosecant patterns. Thirdly, although mutual coupling is captured in the homogenized macroscopic model, the meta-atoms in the microscopic model are still selected based on their scattering parameters with the local periodic assumption and normal incidence. Further refinement in this avenue will allow for more accurate capture of the mutual coupling between elements yielding better agreement between optimizers. Lastly, the optimized EMMS is quite narrow band as bandwidth was not explicitly optimized for from the beginning. Further work to optimize for a desired bandwidth would be valuable.

ACKNOWLEDGMENT

We would like to thank Prof. George Eleftheriades and Vasileios Ataloglou for many extremely helpful discussions concerning auxiliary fields.

REFERENCES

- [1] A. Epstein and G. V. Eleftheriades, "Arbitrary power-conserving field transformations With passive lossless omega-type bianisotropic metasurfaces," *IEEE Trans. Antennas Propag.*, vol. 64, no. 9, pp. 3880–3895, 2016.
- [2] E. F. Kuester, M. A. Mohamed, M. Piket-May, and C. L. Holloway, "Averaged transition conditions for electromagnetic fields at a metafilm," *IEEE Trans. Antennas Propag.*, vol. 51, no. 10, pp. 2641–2651, oct 2003.
- [3] T. Brown, Y. Vahabzadeh, C. Caloz, and P. Mojabi, "Electromagnetic inversion with local power conservation for metasurface design," *IEEE Antennas Wirel. Propag. Lett.*, vol. 19, no. 8, pp. 1291 – 1295, 2020.
- [4] C. Narendra, T. Brown, and P. Mojabi, "Gradient-based electromagnetic inversion for metasurface design using circuit models," *IEEE Trans. Antennas Propag.*, no. c, pp. 1–1, 2021.
- [5] J. Budhu, E. Michielssen, and A. Grbic, "The design of dual band stacked metasurfaces using integral equations," *IEEE Trans. Antennas Propag. (Early Access)*, pp. 1–13, 2022.
- [6] J. Budhu and A. Grbic, "Fast and accurate optimization of metasurfaces with gradient descent and the woodbury matrix identity," in *2021 International Applied Computational Electromagnetics Society Symposium (ACES)*. Hamilton, ON: IEEE, 2021, pp. 1–10.
- [7] V. G. Ataloglou and G. V. Eleftheriades, "Efficient aperture illumination and beamforming with Huygens' metasurfaces exciting surface waves," *15th Eur. Conf. Antennas Propagation, EuCAP 2021*, 2021.

- [8] —, “Arbitrary wave transformations with Huygens’ metasurfaces through surface-wave optimization,” *IEEE Antennas and Wireless Propagation Letters*, vol. 20, no. 9, pp. 1750–1754, 2021.
- [9] G. Xu, V. G. Ataloglou, S. V. Hum, and G. V. Eleftheriades, “Extreme beam-forming with impedance metasurfaces featuring embedded sources and auxiliary surface wave optimization,” *arXiv preprint*, pp. 1–13, 2021. [Online]. Available: <http://arxiv.org/abs/2112.12700>
- [10] R. Gómez-Bombarelli, J. N. Wei, D. Duvenaud, J. M. Hernández-Lobato, B. Sánchez-Lengeling, D. Sheberla, J. Aguilera-Iparraguirre, T. D. Hirzel, R. P. Adams, and A. Aspuru-Guzik, “Automatic chemical design using a data-driven continuous representation of molecules,” *ACS Central Science*, vol. 4, no. 2, pp. 268–276, 2018, pMID: 29532027.
- [11] D. R. Prado, J. A. López-Fernández, G. Barquero, M. Arrebola, and F. Las-Heras, “Fast and accurate modeling of dual-polarized reflectarray unit cells using support vector machines,” *IEEE Trans. Antennas Propag.*, vol. 66, no. 3, pp. 1258–1270, 2018.
- [12] T. Qiu, X. Shi, J. Wang, Y. Li, S. Qu, Q. Cheng, T. Cui, and S. Sui, “Deep learning: A rapid and efficient route to automatic metasurface design,” *Advanced Science*, vol. 6, no. 12, p. 1900128, 2019.
- [13] V. Richard, R. Loison, R. Gillard, H. Legay, and M. Romier, “Loss analysis of a reflectarray cell using ANNs with accurate magnitude prediction,” in *2017 11th European Conference on Antennas and Propagation (EuCAP)*, 2017, pp. 2396–2399.
- [14] D. Kampouridou and A. Feresidis, “Machine learning-driven design optimization for a multi-layer metasurface antenna,” in *2020 14th European Conference on Antennas and Propagation (EuCAP)*, 2020, pp. 2396–2399.
- [15] D. Caputo, A. Pirisi, M. Mussetta, A. Freni, P. Pirinoli, and R. Zich, “Neural network characterization of microstrip patches for reflectarray optimization,” in *2009 3rd European Conference on Antennas and Propagation*, 2009, pp. 2520–2522.
- [16] P. Robustillo, J. Zapata, J. A. Encinar, and J. Rubio, “ANN characterization of multi-layer reflectarray elements for contoured-beam space antennas in the Ku-band,” *IEEE Trans. Antennas Propag.*, vol. 60, no. 7, pp. 3205–3214, 2012.
- [17] M. Salucci, L. Tenuti, G. Oliveri, and A. Massa, “Efficient prediction of the em response of reflectarray antenna elements by an advanced statistical learning method,” *IEEE Trans. Antennas Propag.*, vol. 66, no. 8, pp. 3995–4007, 2018.
- [18] Z. Liu, D. Zhu, S. P. Rodrigues, K.-T. Lee, and W. Cai, “Generative model for the inverse design of metasurfaces,” *Nano Letters*, vol. 18, no. 10, pp. 6570–6576, 2018, pMID: 30207735.
- [19] X. Shi, T. Qiu, J. Wang, X. Zhao, and S. Qu, “Metasurface inverse design using machine learning approaches,” *Journal of Physics D: Applied Physics*, vol. 53, no. 27, p. 275105, may 2020.
- [20] J. Jiang and J. A. Fan, “Global optimization of dielectric metasurfaces using a physics-driven neural network,” *Nano Lett.*, vol. 19, no. 8, pp. 5366–5372, 2019.
- [21] —, “Simulator-based training of generative neural networks for the inverse design of metasurfaces,” *Nanophotonics*, 2019.
- [22] S. An, B. Zheng, H. Tang, M. Y. Shalaginov, L. Zhou, H. Li, M. Kang, K. A. Richardson, T. Gu, J. Hu, C. Fowler, and H. Zhang, “Multifunctional metasurface design with a generative adversarial network,” *Advanced Optical Materials*, vol. 9, no. 5, p. 2001433, 2021.
- [23] W. Ma, F. Cheng, Y. Xu, Q. Wen, and Y. Liu, “Probabilistic representation and inverse design of metamaterials based on a deep generative model with semi-supervised learning strategy,” *Advanced Materials*, vol. 31, no. 35, p. 1901111, 2019.
- [24] G. S. Gosal, “The use of inverse neural networks in the fast design of printed lens antennas,” Ph.D. dissertation, University of Ottawa, 2015.
- [25] G. Gosal, E. Almajali, D. McNamara, and M. Yagoub, “Transmitarray antenna design using forward and inverse neural network modeling,” *IEEE Antennas and Wireless Propagation Letters*, vol. 15, pp. 1483–1486, 2016.
- [26] G. Oliveri, A. Gelmini, A. Polo, N. Anselmi, and A. Massa, “System-by-design multiscale synthesis of task-oriented reflectarrays,” *IEEE Trans. Antennas Propag.*, vol. 68, no. 4, pp. 2867–2882, 2020.
- [27] C. Yeung, J.-M. Tsai, B. King, B. Pham, D. Ho, J. Liang, M. W. Knight, and A. P. Raman, “Multiplexed supercell metasurface design and optimization with tandem residual networks,” *Nanophotonics*, vol. 10, no. 3, pp. 1133–1143, 2021.
- [28] P. Naseri and S. V. Hum, “A generative machine learning-based approach for inverse design of multilayer metasurfaces,” *IEEE Trans. Antennas Propag.*, vol. 69, no. 9, pp. 5725–5739, 2021.
- [29] J. A. Hodge, K. V. Mishra, and A. A. Zaghoul, “Multi-discriminator distributed generative model for multi-layer RF metasurface discovery,” *2019 IEEE Global Conference on Signal and Information Processing (GlobalSIP)*, pp. 1–5, Nov. 2019.
- [30] —, “Deep inverse design of reconfigurable metasurfaces for future communications,” *arXiv preprint*, pp. 1–7, 2021. [Online]. Available: <https://arxiv.org/abs/2101.09131>
- [31] C. Pfeiffer and A. Grbic, “Bianisotropic metasurfaces for optimal polarization control: Analysis and synthesis,” *Phys. Rev. Appl.*, vol. 2, no. 4, pp. 1–11, 2014.
- [32] P. Naseri, S. Pearson, Z. Wang, and S. V. Hum, “A Combined Machine-Learning / Optimization-Based Approach for Inverse Design of Nonuniform Bianisotropic Metasurfaces,” *IEEE Trans. Antennas Propag.* (Early Access), pp. 1–14, Dec. 2021.
- [33] S. Pearson and S. V. Hum, “Optimization of electromagnetic metasurface parameters satisfying far-field criteria,” *IEEE Trans. Antennas Propag.* (Early Access), pp. 1–13, 2021.
- [34] A. Epstein and G. V. Eleftheriades, “Synthesis of Passive Lossless Metasurfaces Using Auxiliary Fields for Reflectionless Beam Splitting and Perfect Reflection,” *Phys. Rev. Lett.*, vol. 117, no. 25, 2016.
- [35] V. G. Ataloglou, A. H. Dorrah, and G. V. Eleftheriades, “Realizing antenna arrays with Huygens’ metasurface pairs based on a moment-method-like design,” *14th Eur. Conf. Antennas Propagation, EuCAP 2020*, 2020.
- [36] M. Salucci, A. Gelmini, G. Oliveri, N. Anselmi, and A. Massa, “Synthesis of shaped beam reflectarrays with constrained geometry by exploiting nonradiating surface currents,” *IEEE Trans. Antennas Propag.*, vol. 66, no. 11, pp. 5805–5817, 2018.
- [37] D. P. Kingma and J. Ba, “Adam: a method for stochastic optimization,” in *3rd International Conference on Learning Representations, ICLR 2015, San Diego, CA, USA, May 7-9, 2015, Conference Track Proceedings*, Y. Bengio and Y. LeCun, Eds., 2015.
- [38] D. Rumelhart, G. Hinton, and R. Williams, “Learning representations by back-propagating errors,” *Nature*, vol. 323, p. 533–536, 1986.
- [39] M. Zebrowski, “Reflectarray antennas illumination and spillover efficiency calculations for rectangular reflectarray antennas,” 2013, pp. 28–38.